Comparative targeting and imaging of atherosclerotic plaque with ultrasmall calcium carbonate nanoparticles

Lydia Martínez-Parra, Marina Piñol-Cancer, Carlos Sanchez-Cano, Ana Miguel-Coello, Desirè Di Silvio, Ana Gomez, Clara Uriel, Sandra Plaza-García, Marta Gallego, Raquel Pazos, et al.

Comparative targeting and imaging of atherosclerotic plaque with ultrasmall calcium carbonate nanoparticles

Lydia Martínez-Parra,[a,b,†] Marina Piñol-Cancer,[a,b,c,†] Carlos Sánchez-Cano,[d,e,f] Ana B. Miguel-Coello,[a] Desiré Di Silvio,[a] Ana M. Gómez,[g] Clara Uriel,[g] Sandra Plaza,[a] Marta Gallego,[a] Raquel Pazos,[a] Hugo Groult,[h] Marc Jeannin,[h] Kalotina Geraki,[i] Laura Fernández Méndez,[a,b,c] Ainhize Urkola,[a] María J. Sánchez Guisado,[a,b] Wolfgang Parak,[j] Mauricio Prato,[a,e,k] Fernando Herranz,[l] Jacob F. Benton,[m,n] Jesús Ruíz-Cabello,[a,c,e,o*] Susana Carregal-Romero[a,c,e*]

[a]Center for Cooperative Research in Biomaterials (CIC biomaGUNE), Basque Research and Technology Alliance (BRTA), 20014 Donostia, Spain
[b]University of the Basque Country (UPV/ EHU), 20018 Donostia
[c]CIBER de Enfermedades Respiratorias (CIBERES), 28029 Madrid, Spain
[d]Donostia International Physics Center, Paseo Manuel de Lardizabal 4, Donostia, 20018, Spain
[e]Ikerbasque, Basque Foundation for Science, 48013 Bilbao, Spain
[f]Polimero eta Material Aurreratuak: Fisika, Kimika eta Teknologia, Kimika Fakultatea, Euskal Herriko Unibertsitatea UPV/EHU, 20018 Donostia, Spain
[g]Instituto de Química Orgánica General, IQOG-SCIC, 28006 Madrid, Spain
[h]BCBS team (Biotechnologies et Chimie des Bioressources pour la Santé), LIENSs Laboratory (Littoral environment et Sociétés), UMR CNRS 7266, 17000 La Rochelle, France
[i]Diamond Light Source, Harwell, Didcot OX11 0DE, United Kingdom
[j]Center for Hybrid Nanostructures (CHyN), Universität Hamburg, 22607 Hamburg, Germany
[k]Dipartimento di Scienze Chimiche e Farmaceutiche, Università degli Studi di Trieste, Trieste, Italy.
[l]NanoMedMol, Instituto de Química Médica, Consejo Superior de Investigaciones Científicas (IQM-CSIC), Madrid 28006, Spain
[m]Experimental Pathology of Atherosclerosis, Centro Nacional de Investigaciones Cardiovasculares Carlos III, 28029 Madrid, Spain
[n]Heart Diseases and Steno Diabetes Center Aarhus, Department of Clinical Medicine, Aarhus University, 8200 Aarhus, Denmark
[o]Departamento de Química en Ciencias Farmacéuticas, Universidad Complutense de Madrid, 28040 Madrid, Spain

† equal contribution
* e-mail: jruizcabello@cicbiomagune.es, scarregal@cicbiomagune.es

Keywords: Atherosclerosis, ligand-mediated targeted imaging, amorphous calcium carbonate nanoparticles, MRI, inflammation, microcalcifications

Abstract

Atherosclerotic plaques present key distinctive features that can provide information on the quiescent state of the plaque or its early disruption triggering fatal events such as myocardial infarction or ischemic stroke. However, to date there are no effective diagnostic tools that provide information on plaque vulnerability, which could improve patients' life expectancy. Conventional protocols lack specificity and fail to predict plaque risk Therefore, new technologies are emerging to overcome this life threating issue. The most promising ones are based on non-invasive medical imaging of the atheroma plaque with customized nanoparticles. Nanoimaging can provide unlimited flexibility to modulate both biological interactions and contrast in different techniques such as magnetic resonance imaging. However, there are few examples that provide comparative studies between nanoparticles targeting different hallmarks of atherosclerosis towards providing information on plaque vulnerability. The aim of our work is to demonstrate that Gd (III)-doped amorphous calcium carbonate nanoparticles are an effective tool for this comparative studies due to their unprecedented magnetic resonance contrast and their physicochemical properties. Herein we compare, in an animal model of atherosclerosis, the imaging performance of three types of nanoparticles; bare amorphous calcium carbonate and those functionalized with the ligands alendronate (for microcalcification targeting) and tri-mannose (for inflammation targeting). The combination of *in vivo* imaging, *ex vivo* tissue analysis and *in vitro* targeting experiments provided useful insights about ligand-mediated targeted imaging of atherosclerosis.

1. Introduction

Atherosclerosis is a chronic inflammatory disease and the origin of most coronary heart pathologies, which in turn are among the leading causes of death worldwide.[1] It consists of lesions in the walls of the arteries, called plaques, composed of fat, cholesterol, necrotic cells, calcifications, and other substances.[2] These lesions cause aberrant blood flow and weaken the artery wall, leading to both cardiovascular diseases and possible rupture of the arteries.[3] One of the most worrying aspects of this pathology is the lack of tools for its early diagnosis, as it is often detected after an infarction. Therefore, one of the strategies to reduce mortality is the implementation of novel clinical diagnostic tools. Among them, medical imaging is the gold standard for the non-invasive examination of patients. In this context, nanotechnology is seen as a promising approach for the design of smart contrast agents against atherosclerosis.[4, 5]

Nanoparticles (NPs) can provide enhanced contrast in many different techniques, such as magnetic resonance imaging (MRI),[6] fluorescence imaging,[7] positron emission tomography (PET),[8] or computed tomography (CT).[9] There appears to be consensus that MRI and PET are the most practical and comprehensive imaging methods to date for imaging atheroma plaque *in vivo*.[4, 10] One of the reasons favoring the use of NPs for plaque imaging is that they can accumulate in the atheroma plaque due to the enhanced permeability of the arterial wall.[11-13] Different preclinical models of atherosclerosis have confirmed the unspecific accumulation of liposomes or poly(lactic-co-glycolic acid) (PLGA) NPs in the plaque.[11, 13] However, developing clinical diagnostic tools would require information on the stage of plaque development and its vulnerability. In this context, targeted imaging with NPs could reveal processes such as enlargement of the necrotic core, presence of microcalcifications or reduction of the fibrotic cap.[10, 14, 15] Therefore, much scientific effort is focused in this direction.

To date, strategies such as ligand-mediated targeting and the use of biomimetic nanoparticle coatings have been applied to image atherosclerotic hallmarks.[12, 15] However, most of these pioneering nanostructures have remained at the preclinical stage due to different drawbacks such as insufficient targeting efficiency or contrast.[10] The practical feasibility of nanotechnology still needs to be determined in assays comparing different parameters such as ligand type, targeted tags and time-dependent accumulation.[10] Furthermore, these assays should take into account sustainable and scalable production of NPs and their biosafety. Otherwise, the transformation of these technologies into clinical settings will be doomed to a dead end.[16]

In this work, we propose the use of advanced MRI contrast agents based on ultrasmall amorphous calcium carbonate (CC) NPs doped with Gd as a robust nanotool for comparative studies of targeted imaging in atherosclerosis. In nature, amorphous CC NPs are precursors in the formation of biogenic calcium carbonate, a major component of rocks, skeletons, or shells.[17, 18] The interest in recent years in creating bio-inspired materials has provided protocols for the synthesis of these transient NPs that ensure colloidal stability by trapping different polyacids such as poly(acrylic acid) (PAA) and citric acid.[17, 19-21] Interestingly, these polyacids act as chelating agents for Gd(III) ions and provide a highly hydrated nanoenvironment that considerably increases their longitudinal magnetic relaxivity. As a consequence, this type of NP presents an unusual increase of contrast in MRI. So far, Gd doped amorphous CC NPs have been applied for *in vivo* studies of NP biodistribution and contrast enhanced MR angiography.[21, 22]

Here, we demonstrate that it is possible to apply these novel contrast agents in targeted imaging of atherosclerosis. First, using a fast and cost-efficient synthesis, we produced amorphous calcium carbonate NPs with enhanced MRI contrast. Then, we covalently bound to these CC NPs two kinds of ligands for either targeting microcalcifications using alendronate, or inflammation through tri-mannose ligands. After that, we compared the performance of the three NPs (bare and with the two ligands) for imaging the atheroma plaque of LDLr-/- mice using MRI. To delve deeper into fundamental aspects of NP targeted imaging, we completed our study with synchrotron X-ray fluorescence (SXRF) analysis of arterial tissue. This technique that allowed us obtaining elemental information of the targeted atheroma plaques and NP location in the aortic tissue,[23] revealed contrary behaviors in the temporal accumulation of NPs functionalized with different ligands, which provided new insights in the field of targeted imaging of atherosclerosis.

2. Results and Discussion

2.1. Synthesis and characterization of MRI nanoprobes for targeted imaging of atherosclerosis.

The synthesis of the different functional MR nanoprobes is shown in **Scheme 1**a. We prepared Gd^{3+} doped ultrasmall CC NPs for ligand-mediated imaging of either calcifications or macrophage presence (see **Scheme 1**b) using a two-step protocol and amino terminated ligands (**Figure S1-8)**. First, Gd-doped CC NPs were prepared by mixing at room temperature $CaCl_2$, $GdCl_3 \cdot 6H_2O$, PAA and Na_2CO_3 for one minute and stopping the particle growth with the addition of ethanol to the reaction solution as it has been previously reported.[22] Then, the unreacted species were separated from the nanoparticles by filtration and, finally, CC NPs were freeze-dried for further use obtaining 2.2 g of nanoparticles with a 3.4 ± 0.2 wt % of Gd. **Figure 2**a and **Figure S9** provide AFM, TEM and STEM images of the obtained CC-NPs which size was 2-3 nm. Subsequently, we covalently bound to the surface of the CC NPs, the two different ligands with amino-terminal domains alendronate and tri-mannose via EDC chemistry (**Scheme 1**a). The synthesis of customized amino-terminated branched tri-mannoside is extensively described in the supporting information (**Figure S1-7**). Alendronate (Aln) is a bisphosphonate ligand known to bind hydroxyapatite (HAP) (**Figure S8**), the main component of the calcifications found in the atheroma plaque. In contrast, functionalization with tri-mannose (Trm) aims to target mannose receptors widely expressed on macrophages and present in the plaque due the inflammation of the artery (**Scheme 1**b).[24]

After the ligand conjugation, CC NPs were characterized by different techniques. First, we determined the number of ligands per weight of nanoparticles by the Rouser method for phosphorous determination (Aln) and, liquid chromatography-mass spectrometry (Trm).[25] The number of Aln and Trm bound to 1 mg of CC NPs were 0.14 ± 0.01 μmol and 0.04 ± 0.01 μmol respectively, corresponding approximately to 1 mannose unit per molecule of Aln. The weight percentage of Gd in each type of nanoprobe was calculated by inductively coupled plasma mass spectrometry (ICP-MS), being 3 wt % in all of them.

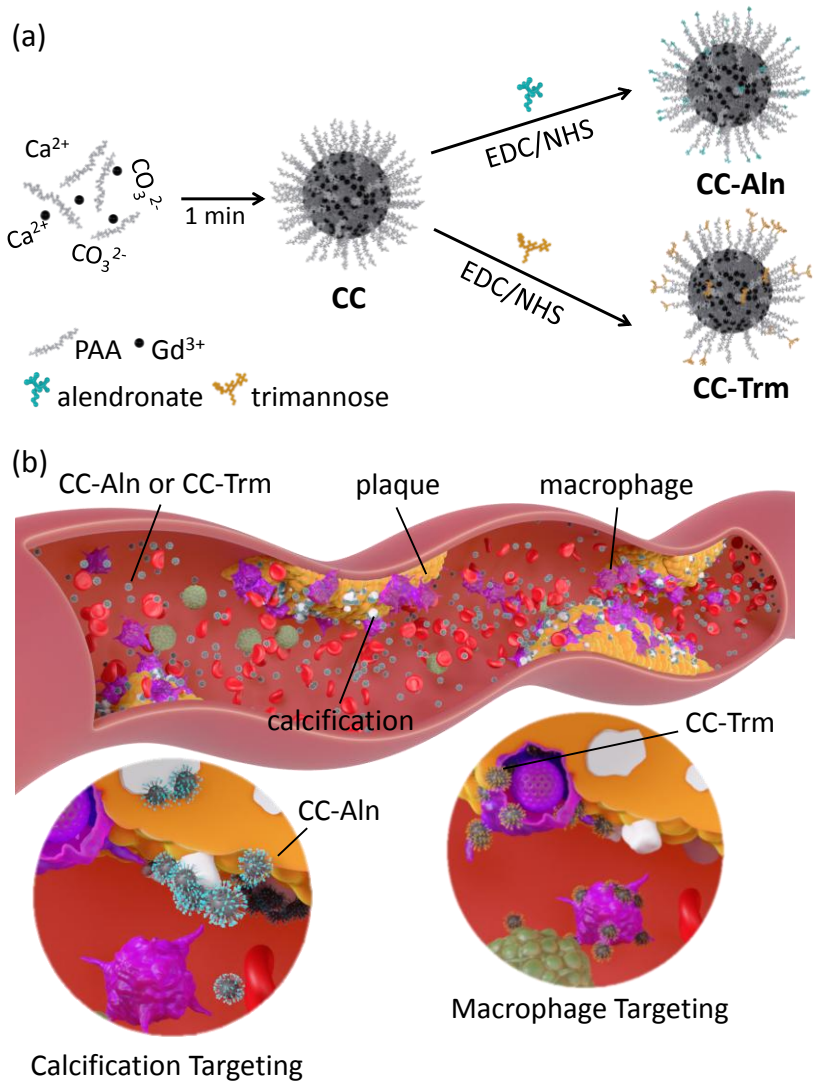

Scheme 1. (a) Schematic illustration of the synthesis protocol of CC-Aln and CC-Trm. (b) Illustration of the ligand-mediated accumulation of CC-Aln and CC-Trm in atheroma plaque via high affinity binding to calcifications and macrophages, respectively.

To evaluate the stability of the ligand-functionalized CC NPs, we compared their size with bare CC NPs by atomic force microscopy (AFM) imaging (**Figure 1**b). Results showed a slight increase in size due to the presence of the ligands between CC and CC-Aln or CC-Trm NPs: CC (2.3 ± 0.3 nm), CC-Aln (3.7 ± 2.4 nm) and CC-Trm (6.6 ± 1.8 nm). This shift was confirmed by dynamic light scattering (DLS) and was accompanied by a decrease of the zeta potential at physiological pH 7.4 shown in **Figure 1**b-c. After ligand functionalization, colloidal stability was ensured for at least eight days as shown in **Figure 1**d but it was not possible to freeze-dry the samples for long-term storage contrary to CC NPs. We further characterized the samples before and after ligand binding by Raman

spectroscopy, Fourier transform infrared spectroscopy (FT-IR), x-ray photoelectron spectroscopy (XPS) and thermogravimetric analysis (TGA).

μ-Raman spectrometry recorded at a 532 nm excitation wavelength confirmed the composition of the different NPs and the stability of the amorphous CC structure after surface modification with Aln and Trm. **Figure 1**e compares the Raman spectra of Gd doped CC NPs, undoped CC NPs, PAA and calcite, the most stable polymorph of $CaCO_3$. It shows how Gd doped CC-NPs exhibited the typical sharp peak of amorphous calcium carbonate centred at 1080 cm^{-1} (black spectrum), which corresponds to the symmetric CO_3^{2-} stretching mode ν_1, with a slight shift when compared with the spectrum of pure calcite (grey spectrum).[26] On the other hand, the lower wavelengths of calcite that arise from the ν_4-asymmetric internal streching mode at 714 cm^{-1} and the lattice mode of the calcite at 155 and 280 cm^{-1} were not retrieved.[27] CC-NPs spectrum also revealed a high proportion of the PAA organic coating (blue spectrum) bound to Na^+ cations. The PAA vibration modes at 1590 cm^{-1} (ν-asymmetric COO^-, carbonyl group), 1461 cm^{-1} (CH_2 deformation), 1422 cm^{-1} (ν-symmetric COO^-), 1331 cm^{-1} (CH_2 twist), 903 cm^{-1} (C-COO^- stretch) and 872 cm^{-1} (C-COO^- stretch), and 515 cm^{-1} (CCO bending) were clearly detected in the CC NP spectrum (with and without Gd^{3+} doping).[28] Also, the higher ratio between 872 and 903 cm^{-1} peaks intensity may be indicating the presence of PAA bound to Ca^{2+} cations.[28] Samples of CC-NPs incorporating Gd^{3+} led to a similar spectra than the one of non-doped CC-NPs, except that the asymmetric CO salt peak at 1590 cm^{-1} vanished suggesting an interaction between the carbonyl groups and the gadolinium ions. **Figure 1**f shows the spectra of bare Gd doped CC NPs compared with their corresponding Aln and Trm coated analogues. In both cases, peaks from Gd doped CC NPs at 517, 872, 903, 1050, 1080, 1331, 1422, and 1461 cm^{-1} were also observed in the Aln-CC and Trm-CC NP spectra meaning that the amorphous structure was maintained. However, although some new peaks appeared in the Raman spectra (at 325, 411, 619, 680, 786, etc.), they could not be unequivocally associated with their corresponding ligand. FT-IR spectra (**Figure 1**g) further confirmed the presence of PAA and the amorphous structure in all three CC, CC-Aln and CC-Trm NPs. Shoulders at 2942 cm^{-1} and 1714 cm^{-1} were associated with the stretching modes of $–CH_2–$ and $–COO^-$ groups, indicative of PAA presence. The split bands at 1415 and 1454 cm^{-1} in the three spectra were assigned to the asymmetric stretching vibration of carbonate ions in amorphous structures.[21, 22] In addition, the phosphate group of alendronate was visible at 1050 cm^{-1} in the CC-Aln sample and the peak at 1200 cm^{-1} in the sample CC-Trm could be assigned to the –C-O groups of Trm.[29] **Figure S10** provides the FT-IR spectra of Aln and Trm. The XPS analysis confirmed the presence of Gd, carbonate and carboxylic groups in the three samples (**Figure S11** and **Table S1**). The elemental analysis of the N 1s core level showed the presence of the amino

terminated ligands Aln and Trm in the CC-Aln and CC-Trm NPs (**Figure 1**h). TGA data (**Figure 1**i) showed a loss around 16 wt % upon heating to 230 ºC (CC 15 %, CC-Aln 15 % and CC-Trm 17 %) due to the dehydration of the amorphous CC core. This value was similar to reported data of amorphous CC NPs. The main release step of all samples is at 450 ºC corresponding to the decomposition process of PAA as it indicated the weight loss derivative analysis of PAA and the three nanoprobes (**Figure S12**). The decomposition of the ligands Aln and Trm can be related with the smooth steps at 259 ºC and 286 ºC, respectively.

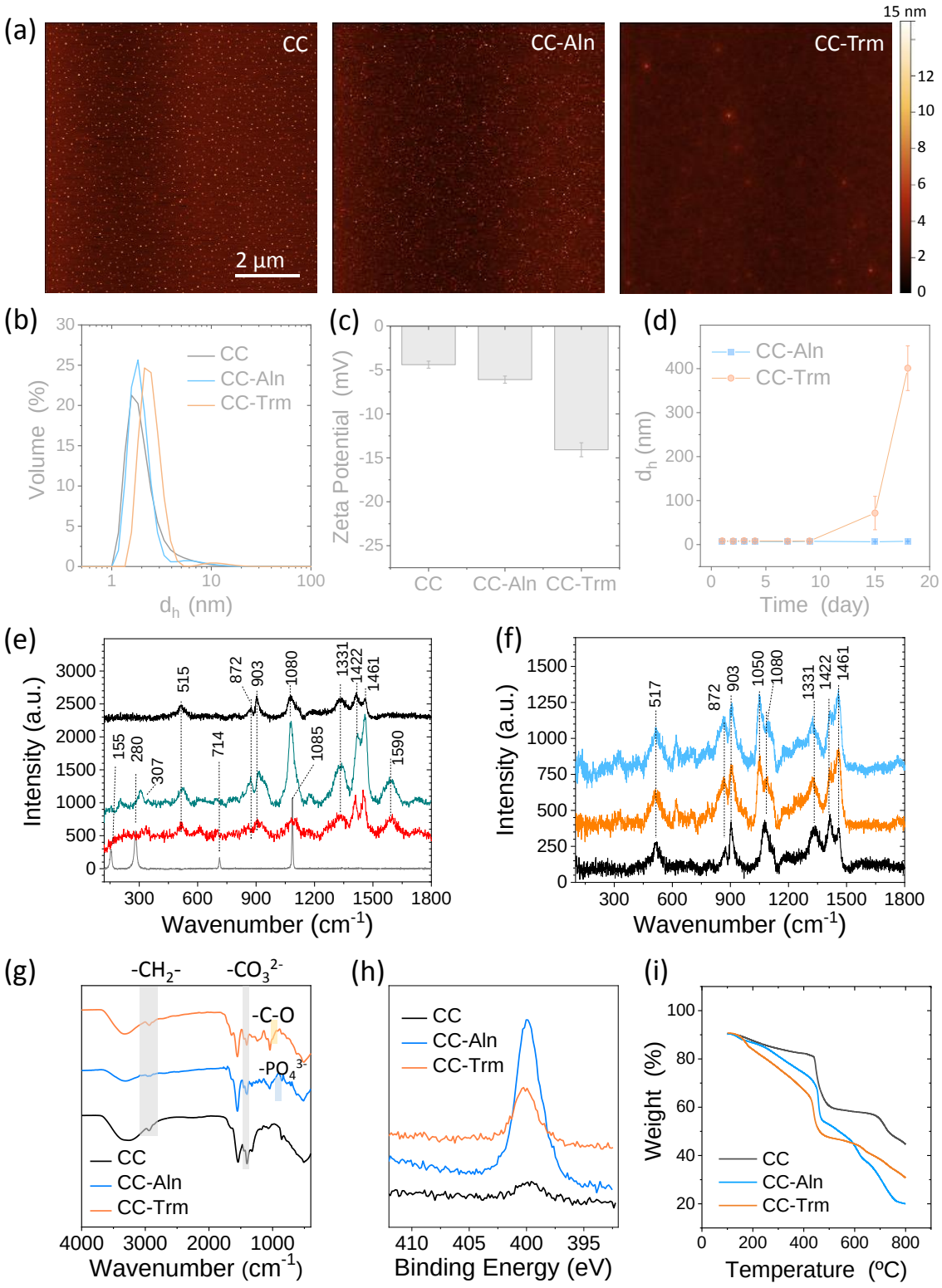

Figure 1. Characterization of targeted CC nanoprobes. (a) AFM images of Gd-doped amorphous CC NPs before and after Aln and Trm functionalization. (b) Hydrodynamic diameter (d_h) (b) and zeta potential (c) measurements of the three NPs. (d) Time dependent colloidal stability of CC-Aln and CC-Trm after their covalent binding to the CC NP surface. (e) µ-Raman spectra recorded at a 532 nm excitation wavelength of calcite (grey), PAA (red), undoped CC NPs (green) and Gd-doped CC NPs (black). (f) µ-Raman spectra of

Gd-doped CC NPs (black), CC-Aln NPs(blue) and CC-Trm NPs (orange) (g) FT-IR spectra of CC, CC-Aln and CC-Trm NPs. (h) Core-level XPS spectra of N 1s. (i) TGA of sample powders with a heating rate of 10 ºC min^{-1}.

High magnetic relaxivity of targeted MRI nanoprobes. Gd-doped amorphous CC NPs are excellent MR contrast agents due to the unusually high longitudinal relaxivity (r_1).[21, 22] Their positive MR contrast far exceeds that obtained with most of commercial Gd-based contrast agents and even the r_1 of ultrasmall iron oxide-based NPs.[6, 30, 31] This is due to the high hydration and confinement of the gadolinium cations within amorphous CC environment. To our knowledge, this type of contrast agents has not yet been decorated with targeting motifs. Since this could trigger the decay of the MR contrast, as it has been previously observed in other type of nanoparticles,[32] the influence of chemical modifications in the surface of CC NPs on their magnetic relaxivity must be studied. To this aim, the longitudinal (T_1) and transversal (T_2) relaxation times of CC NPs were measured at different concentrations for CC, CC-Aln, and CC-Trm NPs at 1.5 and 7 T in a minispec and in a MRI scanner, respectively (**Figure 2**a-b). **Figure 2**c collects the obtained data of the relaxivity r_1 and the ratio between the transversal and longitudinal relaxivity (r_2/r_1). They are compared with the commercial contrast agent Magnevist (Gd-DTPA, r_1= 4.1 mM^{-1} s^{-1}).[30]All three nanoprobes were efficient T_1 contrast agents due to their high r_1 value and the low r_2/r_1 value. The effect of modifying the CC NP surface decreased the r_1 of CC-Aln and CC-Trm NPs by 27-68 % compared to bared CC. This was probably due to modifications in the Gd^{3+} environment such as the decrease in hydration observed in TGA measurements since the leakage Gd^{3+} was negligible. However, despite of it, the r_1 of Aln and Trm functionalized CC NPs greatly outperforms (> 30 mM^{-1} s^{-1} at 1.5 T) synthetic or commercial contrast agents such as Magnevist (4.1 mM^{-1} s^{-1} at 1.5 T) making them anyway superior contrast agents for MRI.[31]

To assess the suitability of our nanoprobes for *in vivo* studies, we further studied the temporal stability of the MR contrast in blood plasma (**Figure 2**d). We measured the ratio r_2/r_1 of CC-Aln and CC-Trm for several days after being freshly prepared (day 0). We observed a slight increase of r_2/r_1 likely due to the formation of the protein corona as it has been reported.[33, 34] However, this value stayed almost constant for one week and only a slight 1.2-fold and 1.1-fold increase was observed for CC-Aln and CC-Trim, respectively, meaning that the positive MR contrast was not impaired due to the protein corona formation and no substantial colloidal aggregation had occurred. Previous studies with positive MR contrast agents have shown that the lack of colloidal stability generates a much larger increase in the r_2/r_1 ratio ($\Delta r_2/r_1$ > 20 times).[34]

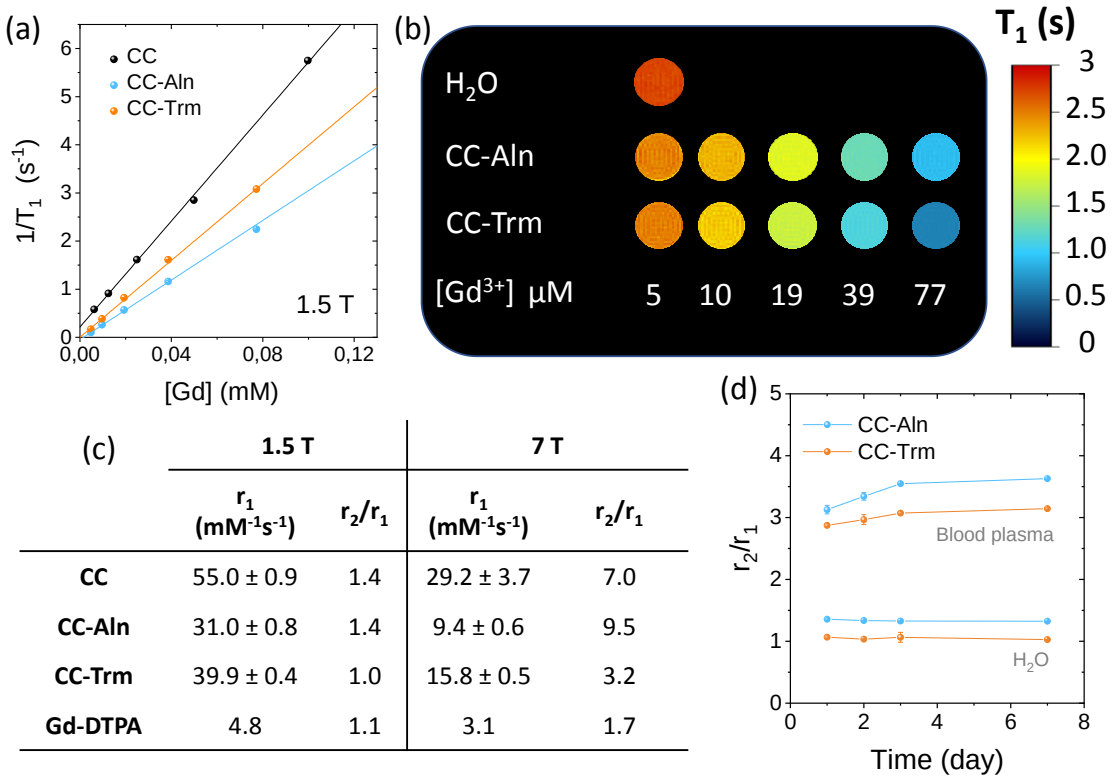

(c)

	1.5 T		7 T	
	r_1 ($mM^{-1}s^{-1}$)	r_2/r_1	r_1 ($mM^{-1}s^{-1}$)	r_2/r_1
CC	55.0 ± 0.9	1.4	29.2 ± 3.7	7.0
CC-Aln	31.0 ± 0.8	1.4	9.4 ± 0.6	9.5
CC-Trm	39.9 ± 0.4	1.0	15.8 ± 0.5	3.2
Gd-DTPA	4.8	1.1	3.1	1.7

Figure 2. **MR contrast of targeted CC NPs.** (a) Plot of $1/T_1$ versus Gd concentration for CC, CC-Aln and CC-Trm NPs at 1.5 T (n=3). (b) Concentration dependence of the T_1 contrast obtained in a MRI scanner at 7 T. (c) Table of longitudinal relaxivity (r_1) data and ratio r_2/r_1 of the different nanoprobes at 1.5 and 7 T. Longitudinal stability of the relaxometric properties in different water and blood plasma (d).

Biosafety and biodistribution. Gd-based contrast agents are among the most widely used contrast agents in medical imaging. Forty percent of clinical MRI scans are performed with this type of contrast. However, free Gd^{3+} can be toxic if it is not properly chelated or if it accumulates in the body over the long-term.[35] To assess the biosafety of our nanoprobes, we studied both the stability of the Gd within the NPs and the cell viability and biodistribution. The possible leakage of Gd from the nanoprobes was studied in different media that mimicked biological fluids with CC NPs (**Figure 3**a). These NPs were kept at 37 ºC in water, PBS buffer at pH 7.4, citrate buffer at pH 4.5 and blood plasma for several days and filtered to determine the Gd^{3+} released at different time points. In addition, the ion exchange with Zn^{2+} was also studied in these media. This metal is essential for maintaining cellular homeostasis and is one of the most abundant intracellular metals.[36, 37] Therefore, transmetallation between Gd^{3+} and Zn^{2+} could be detrimental in two directions, due to Gd^{3+} toxicity and due to a modification of the buffering capacity of intracellular Zn that can injure cells.[38] The results showed that only at pH 4.5, the NPs seem to lose their Gd content very rapidly, likely due to

dissolution of the calcium carbonate.[17] To further investigate the effect of pH, in a range between pH 5-7 we studied the Gd leakage of the samples CC, CC-Aln and CC-Trm. **Figure 3**b shows the high stability of all three NPs at pH values as low as pH 4.9 with the measured Gd leakage being less than 0.05 %. This means that in most biological environments these NPs might be stable, including atherosclerotic lesions where the pH ranges from 6.5 to 8.5.[39] Next, we studied cell viability with red blood cells, HepG2 hepatic cells and EA.hy926 vascular endothelial cells after incubation with CC, CC-Aln and CC-nanoprobes. These cell lines were chosen because the MR nanoprobes are designed for intravenous (i.v.) administration, nanoparticles tend to accumulate in the liver and endothelial cells are the most exposed to the lumen in the aortic cell wall. Results (**Figure S13**, **Figure 3**c,d and **Figure S14**a,b) showed the lack of necrotic effects induced by the NPs and no obvious cytotoxicity after 3 and 24 h, even at the highest concentration (10 μg Gd/mL, 1 mg NP/mL). This low cytotoxicity *in vitro* was confirmed at 48 h (**Figure S14**c,d).

Finally, in a healthy murine model (C57BL/6 mice), we investigated the organ biodistribution of the three nanoprobes (at a similar dose of 0.1 mmol Gd/kg mouse) after i.v. administration by MRI. As shown in **Figure 3**e, the highest decrease of T_1 due to the accumulation of NPs was observed in liver, spleen, and kidneys for the three NPs. The accumulation of the three NPs in the kidneys is remarkable and demonstrates a partial renal clearance which is convenient to avoid long-term accumulation of NPs in the body. This was confirmed by ICP-MS analysis of both the organs and urine (**Figure 3**f). Since these experiments were performed at a constant dose of Gd, the higher values of ΔT_1 for CC NPs are reasonable considering their higher r_1 (**Figure 2**). However, the higher Gd accumulation in organs observed in **Figure 3**f could indicate a faster blood clearance of CC NPs with respect to CC-Aln and CC-Trm NPs. The accumulation of Gd in urine only indicates its presence as the heterogeneity of this type of measurement does not allow quantitative comparison. Finally, we confirmed that the accumulation of the three nanoprobes in the aortic wall was negligible in the absence of atherosclerotic plaques (**Figure S15**).

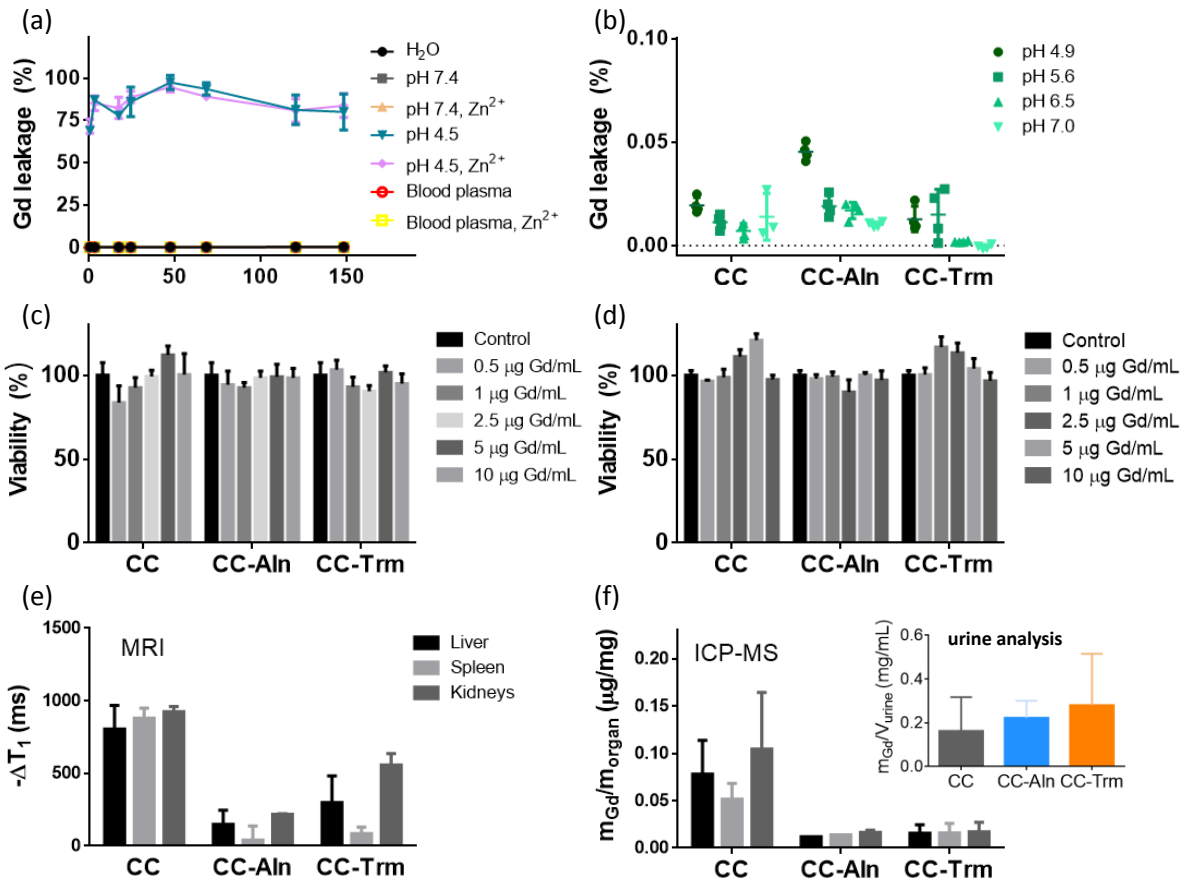

Figure 3. Biosafety and biodistribution. (a) Investigation of the Gd leakage in different media with and without 2.5 mM Zn^{2+}. (b) Stability of Gd (III) entrapped within CC, CC-Aln and CC-Trm NPs at different acidic pH values. (c) Cell viability of HepG2 treated with the three NPs at different concentrations (n= 3). (d) Cell viability of EA.hy926 treated with the three NPs at different concentrations (n= 3). (e) Decrease of positive MRI contrast in the organs where NPs accumulated after i.v. administration. (f) Quantitative analysis of Gd mass in liver, spleen, kidneys and urine per weight of dried tissue.

Comparative study of ligand-mediated targeting in atherosclerosis. After confirming the stability and biosafety of our MR nanoprobes, we verified the targeting and MR imaging ability of CC-Aln and CC-Trim NPs towards microcalcifications and macrophages *in vivo*. We selected these two targets due to their key roles in atherosclerosis.

Microcalcifications, ranging in size from a few to hundreds of microns, composed mainly of HAP ($Ca_5(PO_4)_3(OH)$) are one of the main responsible factors for the loss of elasticity of the atherosclerotic plaque that ultimately triggers its rupture. Therefore, they are related to plaque vulnerability and their medical imaging could be a relevant diagnostic tool.[15] Several previous studies have demonstrated that adapting Ca-targeted NPs proposed for bone applications to image

vascular calcifications can be a successful strategy given the similarities of both biomaterials (both made of HAP).[40] In this context, NPs have been functionalized mainly with Ca-targeting peptides and bisphosphonate ligands. The affinity of bisphosphonates for HAP is due to their chemical resemblance to pyrophosphates, which regulate HAP formation in the body. We selected alendronate for CC functionalization because it is a bisphosphonate ligand that has recently been applied for imaging microcalcifications.[15]

Macrophages are involved in the pathogenesis and progression of atherosclerosis. Therefore, nanoprobes that can specifically target them can provide pivotal insights into both atherosclerosis progression and quantification of atherosclerosis burden. NPs can be designed to target different cell receptors, such as lectin-like oxidized receptor-1 (LOX1), macrophage receptor (MARCO) or macrophage mannose receptor (MMR) expressed on the surface of macrophages can be recognized by targeted NPs. In this context, MMR-targeted ligands have long been applied to enhance the macrophage uptake of NPs.[41] Some of these nanoprobes are already in clinical trials such as dextran coated iron oxide NPs.[4] We decorated the surface of CC NPs with customized mannose ligands, known to enhance macrophage uptake of NPs.[40]

In vivo MR imaging studies were performed with a low-density lipoprotein receptor-deficient (LDLr-/-) mouse model (**Figure 4**a). This mouse model was selected because is one of the most widely employed to study fundamental biological aspects of the disease, new treatments and diagnostic tools.[41, 42] CC-Aln, CC-Trm and bare CC NPs were i.v. administered at a dose of 0.1 mmol Gd/kg. and images of the three groups of animals (n= 3) were registered after 1 h. Then, we analysed the contrast-to-noise-ratio (CNR) of the aortic arch tissue before and after the administration of the three types of NPs (**Figure 4**b,c). This kind of data analysis was chosen because CNR values provide quantitative information on signal-to-noise ratio (SNR) enhancement and targeted imaging efficacy taking into account the background signal. CNR enhancement with contrast agents increases the perception of distinct differences between tissues and biological events such as inflammation. Moreover, it is a value that can be compared between MRI scanners of different magnetic fields.[43] In our experiments it was defined as the difference between the SNR of the aortic arch tissue and the SNR of the muscle tissue ($CNR= SNR_{AA}-SNR_{M}$). **Figure 4**b shows how the CNR increased after the administration of all three nanoprobes. However, the only MR nanoprobes that provided the greatest and significantly different CNR enhancement due to a ligand targeting effect were CC-Aln NPs. In contrast, the ligand Trm provided a negligible accumulation of the CC-Trm after 1 h. **Figure 4**c shows representative MRI images of the targeted imaging of CC-Aln NPs in the aortic arch tissue that were verified in other segments of the aorta, specifically in the sections near the kidneys (**Figure**

S16). The results also show some accumulation of bare NPs but taking into consideration its higher r_1 value, it can be assumed that the concentration of NPs in the tissue was much lower than CC-Aln. The ability of CC-Aln NPs to image atherosclerotic plaques was further demonstrated with Apoe-/- mice (a well stablished atherosclerotic mice model) as shown in **Figure S17**. With our study, we imaged by MRI the significantly different accumulation of NPs due to ligand-mediated targeting. To our knowledge, comparative studies on ligand-mediated atherosclerosis imaging with NPs are scarce. Kim et al. demonstrated increased accumulation of iron oxide-based contrast agents targeting the plaque neovasculature compared with similar NPs targeting the fibrous cap.[14] However, these results were obtained *ex vivo* by analyzing the aortic tissue after NP administration by fluorescence and MRI. One of the challenges in imaging atherosclerosis is the standardization of contrast agents that allow comparative studies between different biological targets with non-invasive methods such as *in vivo* MRI.[10] Our results indicate that Gd-doped CC NPs are a valid tool in this field thanks to the MRI contrast enhancement and the non-significative accumulation of bare CC NPs within the atheroma plaques which permeability is enhanced respect to healthy aortic tissue.(reF) In order to understand the lower ligand mediated targeting of CC-Trm vs CC-Alen we analysed the aorta tissues by two distinct methods: histology and synchrotron X-ray Fluorescence (SXRF) analysis.

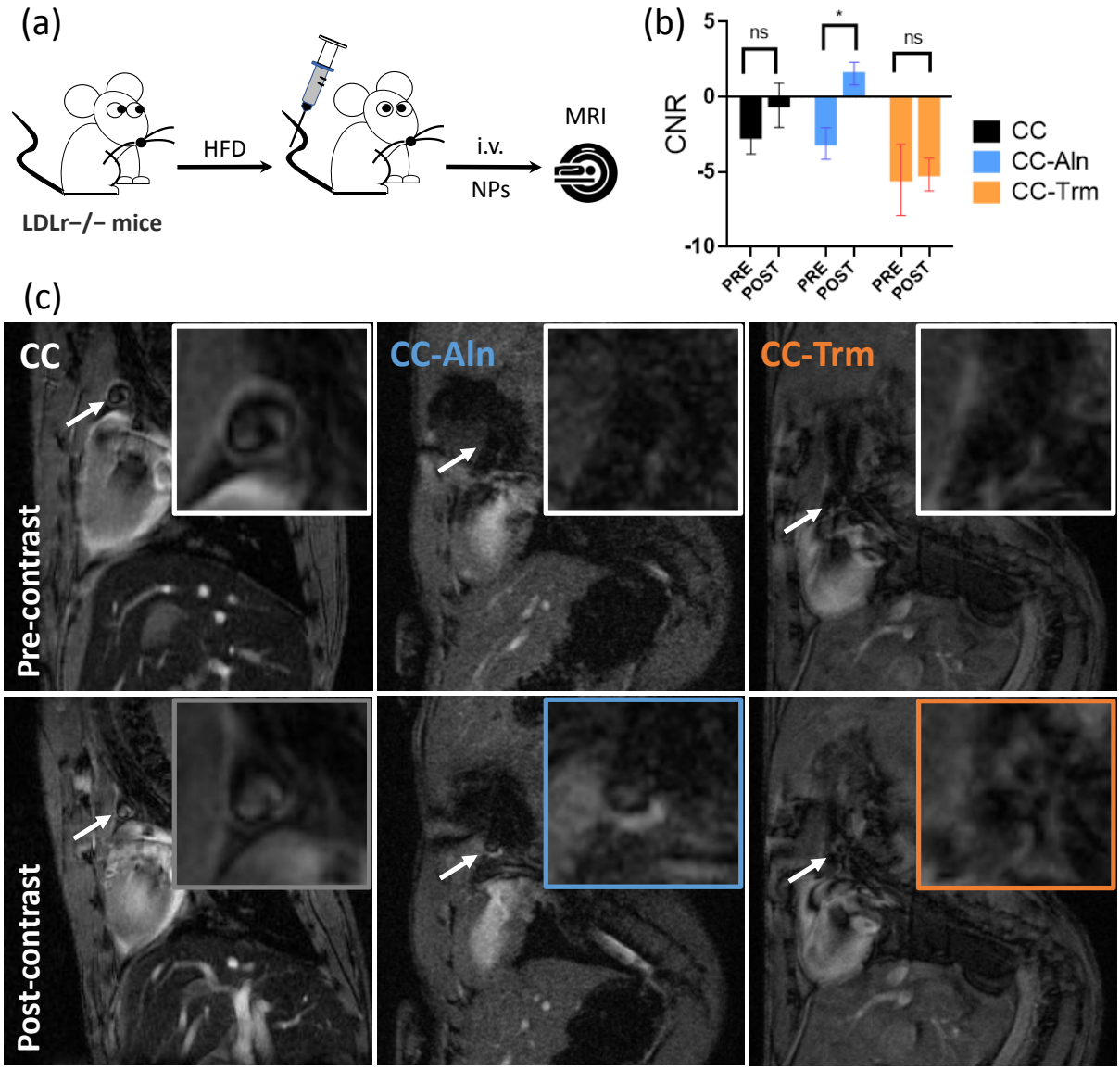

Figure 4. Targeted imaging of atherosclerosis with NPs *in vivo*. (a) Schematic of targeted MRI of atherosclerosis in LDLr-/- mice with amorphous CC NPs functionalized with different ligands (Aln and Trm). (b) Comparison of CNR enhancement of the aortic arch tissue with targeted CC NPs (CC vs CC-Aln and CC-Trm NPs). (c) T_1-weighted MRI before (pre-contrast) and after 1 h (post-contrast) of the i.v. administration of bare CC (grey), CC-Aln (blue) and CC-Trm (orange) NPs. The arrows indicate the position of the aorta, and the insets are magnified images of the aorta. Multiple t-test statistical analysis. *P<0.05, n.s. not significant *P>0.05.

Ex vivo evaluation of ligand-mediated targeted imaging of atherosclerosis

Aortas from LDLr-/- mice treated either with saline solution, or the various CC NPs (CC, CC-Trm or CC-Aln; 0.05 mmol NPs/kg) were extracted and cryopreserved with OCT. Then, both 5 and 50 µm

thick cross sections were generated and deposited either on glass slides for histology or on sapphire discs for *ex vivo* analysis using synchroton X-ray fluorescence (SXRF) analysis. Histology analysis of the aortas confirmed the presence of microcalcifications in our LDLr-/- atherosclerotic mice model through alizarin red staining and polarized light imaging. The presence of macrophages (due to inflammation) was confirmed through a CD68 immunohistochemistry analysis. Data are collected in **Figure S18** (SI).

SXRF maps and spectra (**Figure 5**, **Figure S19-S26**) of aorta areas previously selected by brightfield microscopy were acquired at room temperature at beamline I18 (Diamond Light Source UK), using a beam with the energy set at 11 keV and focused at 5 x 5 μm^2. SXRF is a quantitative analytical method that uses X-rays to excite electrons at the inner orbitals of atoms and obtain distinctive emission signals from each element. When combined with scanning acquisition strategies, it allows generating maps that show the spatial distribution of different elements within a sample.[44, 45] Therefore, it was ideal to provide quantitative information about the ability of the different CC NPs (CC, CC-Trm or CC-Aln) to get accumulated within atherosclerotic arteries. To this aim, we included a second time point (15 min) to explore the temporal dimension in the accumulation of CC NPs (with and without targeting ligand) in the plaque and compared it with untreated mice. As expected, aortas from untreated animals used as controls did not show Gd-related SXRF emission (**Figure 5**a, **Figure S19**). On the contrary, Gd-L fluorescence peaks of different intensity were visible in samples treated with the various CC NPs (**Figure S19**). Initial analysis of the SXRF maps showed that all CC NPs mainly accumulated close to, but not inside, areas with high concentration of Zn (**Figure 5**a, **Figure S20-S26**). Such Zn rich areas are normally associated to cellular tissue, as this metal is highly concentrated in the nuclei of cells.[46, 47] Thus, it seems possible that the particles are getting accumulated in areas around the endothelium of the aortic tissue (as expected if targeting atherosclerotic plaque). Still, bare CC NPs and particles targeting inflammation (CC-Trm NPs) could be observed at short treatment times (average accumulations of 0.82 ± 0.12 and 0.33 ± 0.13 ppm Gd/μm^2 respectively after 15 min treatment) but CC-NPs were removed from the arteries promptly while CC-Trm NPs slightly decrease their concentration (average accumulations of 0.09 ± 0.05 and 0.23 ± 0.10 ppm Gd/μm^2 respectively after 60 min treatment). Instead, CC-Aln NPs modified with alendronate to target microcalcifications accumulated in a progressive manner and in greater quantities (average accumulations of 0.73 ± 0.58 ppm Gd/μm^2 after 15 min treatment, and 1.99 ± 1.31 ppm Gd/μm^2 with multiple areas with more than 10 ppm Gd/μm^2 after 60 min treatment). Therefore, *ex vivo* SXRF experiments were in agreement with results obtained in previous *in vivo*

MRI, confirming that CC-Aln NPs are more efficient and specific at targeting atherosclerotic plaque than the other CC NPs studied (**Figure 5**a-b, **Figure S20-S26**).

Such differences in accumulation and permanence in the aorta of mice could indicate that targeting of microcalcifications with alendronate is directing CC-Aln inside the lipid-rich core of the atherosclerotic plaque, while other particles are not able to reach it and get washed away. This would also explain the increase in correlation between Ca and Gd at longer treatment times observed in mice treated with CC-Aln, and the decrease under the same circumstances observed in animals treated with bare CC or CC-Trm NPs (**Figure 5**c). Unfortunately, all CC NPs are Ca based nanomaterials, so they could increase the Ca-Gd correlation when higher quantities of the NPs are accumulated in a tissue. Therefore, further experiments are needed to confirm if CC-Aln NPs reach microcalcifications inside the atheroma plaque. Interestingly, CC-Trm NPs were not highly accumulated in the atheroma plaque but were not washed out over time. This could either be due to the low presence of macrophages or due inefficient targeting *in vivo*. Further experiments with atherosclerotic animal models with different degrees of inflamed tissue would be needed to further explore the ability of the tri-mannose ligand to target plaque macrophages.

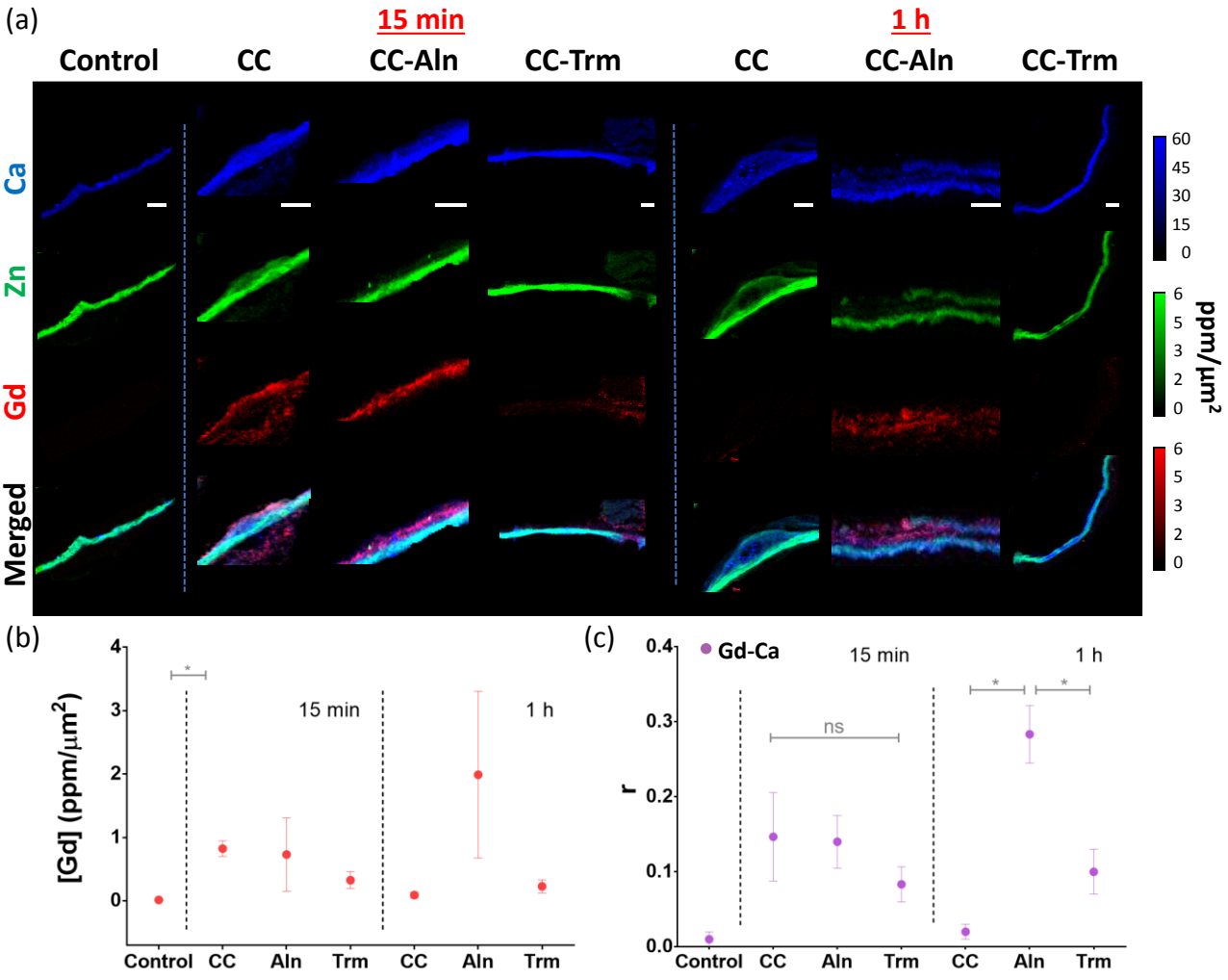

Figure 5. XRF imaging of NPs in atherosclerotic aortas *ex vivo*. (a) Representative SXRF Ca, Zn and Gd elemental and composite maps of 50 μm thick longitudinal sections of aortas from LDLr-/- mice model of atherosclerosis untreated or treated with a single i.v. administration of Gd-doped CC, CC-Trm or CC-Aln NPs (0.05 mmol/kg) for 15 or 60 min, obtained using incident energy 11 keV at 5×5 μm^2 step size; scale bar 500 μm. Images were generated in FIJI ImageJ package.[48] (b) Comparison of average Gd accumulation/area unit (as ppm Gd/μm^2) in the aortic tissue analyzed with SXRF in *(a)*. (c) Ca-Gd correlation (shown as r-Pearson correlation coefficient) in the aortic tissue analyzed with SXRF in (a). Multiple t-test statistical analysis. *P<0.05, n.s. not significant *P>0.05.

In vitro evaluation of ligand-mediated targeting. Thanks to the SXRF analysis of aortic tissue, we observed that the NP blood circulation time possibly favors the specific targeting of CC-Aln NPs in the atheroma plaque, and conversely, impairs the targeting with CC-Trm and the inespecific accumulation of CC-NPs. For this reason, we performed additional targeting studies to determine whether a similar behavior is observed *in vitro*. To evaluate the affinity of CC-Aln for

microcalcifications mainly composed of HAP, we compared the adsorption of CC-Aln, CC and CC-Trm NPs to HAP microparticles at physiological pH (7.4) and at different incubation times (15 min and 1 h, under stirring). After the incubation time and several washing steps, the remaining amount of the various CC NPs (CC, CC-Aln and CC-Trm) still adsorbed on the HAP sample were determined. We used energy-dispersive X-ray spectroscopy (EDX) and ICP-MS to confirm the colocalization of Gd on the HAP surface, which main characteristic atomic components are Ca and P, (**Figure 6**a, **Figure S27**) and calculate the ratio of [Gd]/[Ca] (**Figure 6**b, **Figure S28**), respectively. Both results, at 15 min and 1 h, confirmed a slight increase of the accumulation of NPs with the increase of the incubation time and, a higher presence of CC-NPs on the HAP microparticles compared to CC-Aln and CC-Trm NPs. This could be due to a faster attractive interaction between CC-NPs and HAP that has also been observed *ex vivo* by SXRF at 15 min post-administration (**Figure 5**). At pH 7.4, most of the PAA on the CC NP surface must be dissociated, so CC NPs could be adsorbed on HAP microparticles through electrostatic interactions or through the formation of hydrogen bonds with the OH and PO_4 surface groups of HAP. However, bisphosphonates such as alendronate are known for their high binding affinity to HAP and low reversible adsorption.[49, 50] Possibly, these facts made it possible that, *in vivo*, CC-Aln NPs were not washed out of the atheroma plaque over time, and that the CC-Aln NPs increased their concentration in the aortic tissue enhancing their MR signal and making them the best contrast agents of those tested in this work. Finally, we verified the ability of CC-Trm to target macrophages compared with their counterparts CC and CC-Aln NPs. **Figure 6**c shows a slight increase of their uptake compared to CC and CC-Aln NPs at two different time points (30 min and 2 h) that might not be sufficient to stimulate their specific accumulation in macrophages *in vivo*.

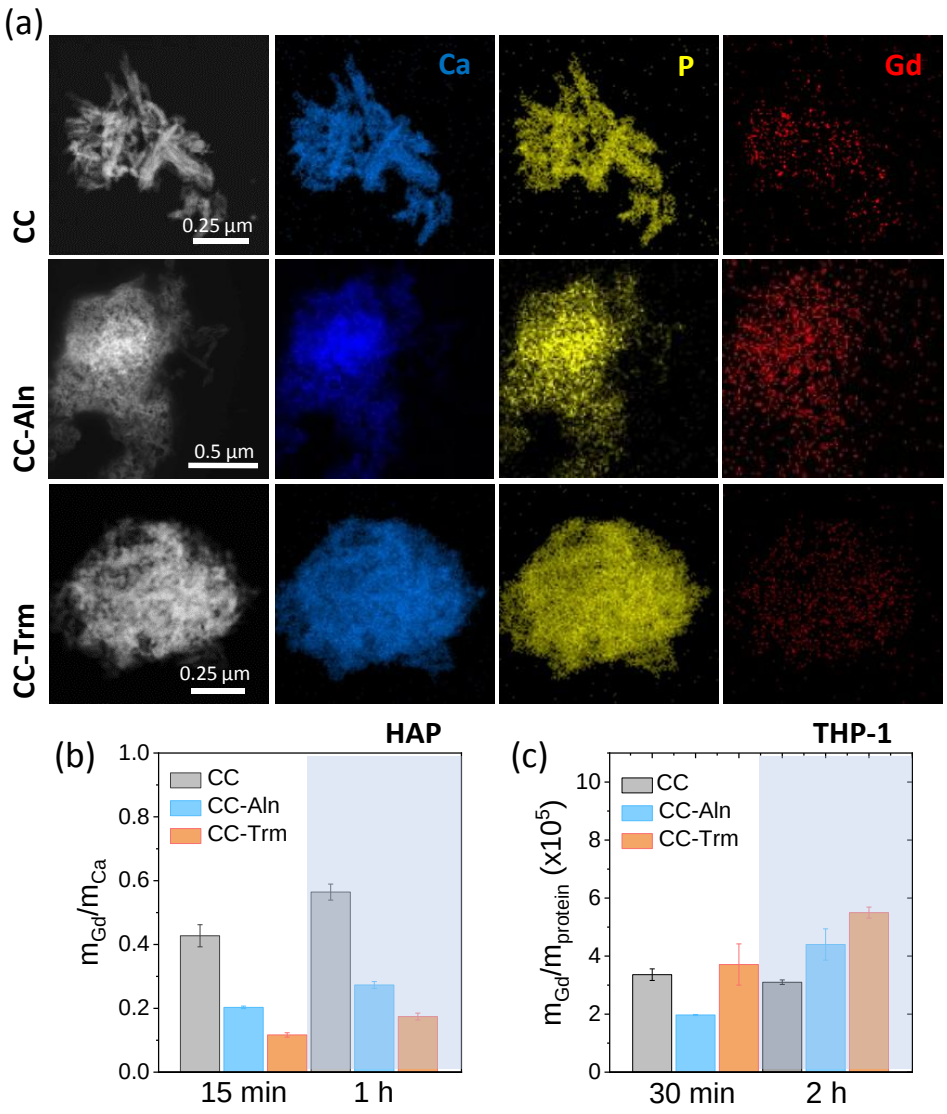

Figure 6. Targeting *in vitro*. EDX analysis of adsorption of CC-Aln for HAP compared to CC-Trm. STEM images of HAP and corresponding element mapping of HAP components (Ca and P) and Gd present in CC-Aln and CC-Trm (a). ICP-MS measurements of Gd adsorbed on the HAP samples after 5 and 15 min of incubation (b). NP uptake studies with THP-1 derived macrophages determining the amount of Gd by ICP-MS per cellular protein.

3. Conclusions

Nanoparticles that detect, by non-invasive methods such as MRI, the different stages of atheroma plaque development may be clinically beneficial. To this aim, it is necessary to develop nanoplatforms that allow their surface modification with different ligands towards targeting the main hallmarks of atherosclerotic lesions *in vivo* and the implementation of analytical techniques that facilitate the understanding of the nano-bio interactions. In this context, we demonstrated that Gd (III)-doped amorphous calcium carbonate nanoparticles are an excellent nano-tool for screening different targeted ligands due to their unprecedented high MRI contrast and their physicochemical properties that provide high Gd stability, easy surface functionalization and partial renal clearance.

In this work, to compare the targeting ability between different ligands, alendronate and tri-mannose were successfully conjugated to Gd (III)-doped amorphous calcium carbonate nanoparticles. These nanoparticles target either microcalcifications or the enhanced presence of macrophages in the plaque. The characterization of the functionalized MRI nanoprobes showed the stability of Gd (III) and the amorphous structure of the nanoparticles, the excellent MRI T_1-contrast of all nanoprobes and the effective targeting ability *in vitro* of the nanoparticles functionalized with alendronate. From the MRI studies and the implementation of synchrotron XRF tissue analysis, we demonstrated that the functionalization of nanoparticles with alendronate provided specificity for atheroma plaque imaging compared to bare nanoparticles that accumulated initially in the plaque but were progressively washed out. The results obtained with the tri-mannose ligand showed an inefficient accumulation of nanoparticles that need to be further explored to decipher whether the concentration of macrophages with the atheroma plaque was not sufficiently high for targeted imaging or the nano-bio interactions were not strong enough.

Our findings obtained by a combination of non-invasive MRI, *in vitro* studies, and *ex vivo* analysis, point at the importance of the binding affinity between the corresponding ligand and the targeted tissue to overcome the blood flow clearance of nanoparticles adsorbed at the epithelium of the aorta. This high binding affinity, in the case of the alendronate ligand, provided the specificity needed to accumulate over time in the atheroma plaque proving a significant increase of the contrast-to-noise-ratio signal in MRI.

Experimental Section

Materials. Anhydrous sodium carbonate ≥99.0 (Na_2CO_3) was purchased from Fluka, Anhydrous calcium chloride 97% ($CaCl_2$) was purchased from Riedel-de Haën, Poly(acrylic acid sodium salt) average Mw ~2100, gadolinium (III) chloride hexahydrate ($GdCl_3 \cdot 6H_2O$), 1-ethyl-3-(3-dimethylaminopropyl) carbodiimide (EDC), N-hydroxysulfosuccinimide sodium salt (sulfoNHS), hydroxyapatite (HAP) and alendronate (Aln) sodium trihydrate were purchased from Sigma-Aldrich. The customized synthesis of the amino-terminated tri-mannose ligand is extensively described in the Supporting Information (SI). All solutions were prepared using nanopure water as solvent (Thermo Scientific™ Barnstead™ Nanopure).

Synthesis of amorphous calcium carbonate nanoparticles doped with gadolinium. CC NPs were prepared according to previous reports with slight modifications mainly in the purification process.[21] Briefly, 686.4 mg of $CaCl_2$ and 7.68 g of poly(acrylic acid) (PAA, Mw~1500) were dissolved and mixed in 60 mL nanopure H_2O water and then mixed with 316.32 mg of $GdCl_3 \cdot 6H_2O$, under vigorous stirring at room temperature. Finally, 60 mL of $NaCO_3$ (10.6 mg/mL) was added and stirred for one minute. To terminate the reaction, 120 mL of ethanol was added. This mixture was centrifuged for 2 min at 3000 rpm once and then, the precipitate was resuspended in 10 mL of nanopure H_2O and washed by ultrafiltration with 3kDa AMICON. All samples were lyophilized and stored at room temperature.

Surface functionalization of CC NPs. Lyophilized CCs (25 mg) were resuspended in water and added to a vial with 26.6 mg of EDC and 32.6 mg of sulfo-NHS. This mixture was stirred for 30 min to activate carboxylic groups. When time was up, ultracentrifugation was performed with 3 kDa AMICON filters (0.5 mL each filter) at 12500 rpm, 20 min. The retentate was resuspended in PBS (0.01 M, pH 8). This suspension was added to a vial with 1 mg of the desired ligand (alendronate or tri-mannose) and left incubating for 1 h at room temperature. Finally, functionalised CCs were purified by ultracentrifugation with kDa AMICON 3 filters to eliminate unreacted species.

Characterization. Atomic force microscopy (AFM) imaging was performed using a Veeco Multimodel AFM attached to a Nanoscope V controller. The samples were imaged in tapping mode in solution, using a V-TESPA probe with k= 42N/m. ICP-MS measurements were performed on a Thermo iCAP Q ICP-MS (Thermo Fisher Scientific GmbH, Bremen, Germany), coupled to an ASX-560 autosampler (CETAC Tech, Omaha, NE, USA). Dynamic Light Scattering (DLS) was performed to measure the hydrodynamic diameter and zeta potential of CCs using a Malvern Zetasizer Nano-ZS (Malvern Instrument, Malvern, UK). Thermogravimetric analyses were

performed under air (25 mL·min−1flow rate) using a TGA Discovery (TA Instruments). The samples were equilibrated at 100°C for 20 min to eliminate humidity and then heated at a rate of 10 °C·min^{-1} from 100 to 800°C. X-ray photoelectron spectroscopy (XPS) experiments were performed in a SPECS Sage HR 100 spectrometer with a non-monochromatic X-ray source (aluminium Kα line of 1486.7 eV energy and 252 W), placed perpendicular to the analyzer axis and calibrated using the $3d_{5/2}$ line of Ag with a full width at half maximum (FWHM) of 1.1 eV.

Magnetic relaxometry. The Magnetic relaxivities of the nanoprobes were measured in a Bruker Minispec MQ60 (Bruker Biospin GmbH) contrast agent analyzer at 1.5 T at 37 ºC. Additionally, T_1 and T_2 were also measured in a 7 T horizontal bore Bruker Biospec USR 70/30 MRI system (Bruker Biospin GmbH). The relaxivities r_1 and r_2 were obtained by plotting 1/T against gadolinium concentration (mM) measured by ICP-MS.

Nanoparticle stability assays. Gd leakage and transmetallation were studied by incubating 1 mg of CC NPs in 0.5 mL with the corresponding buffer (H_2O, PBS pH 7.4, PBS pH 7.4 + Zn^{2+}, citrate buffer pH 4.5 and citrate buffer pH 4.5+ Zn^{2+}), blood plasma, blood plasma + Zn^{2+}, at 37 ºC for different time points. At each time point, samples were filtrated with 3 kDa AMICON filters at 13000 rpm, for 10 min. The filtrates were analyzed by ICP-MS to determine the Gd leakage. The hydrodynamic diameter of the nanoprobes and the magnetic relaxivities were also measured for several days after the synthesis to verify their colloidal and magnetic stability.

Cytotoxicity analysis. First, we analyzed the impact of CC, CC-Aln and CC-Trm NPs on cellular mitochondrial activity using 3-(4,5-dimethylthiazol-2-yl)-2,5-diphenyl tetrazolium bromide (MTT) assay in two cell cultures, EA.hy926 vascular endothelial cells and HepG2 hepatic cells, at three different times (24, 48 and 72 h) and five different NP concentrations (results included in the Supporting Information). Next, we studied whether the observed low cytotoxicity was due to apoptosis or necrosis with the Annexin V Apoptosis Detection Kit APC (Ebioscience™ #88-8007-72). Briefly, EA.hy926 cells (25.000 cells/well) were seeded in 24-well plates one day prior to NP incubation. The three types of NPs were administered to cells at different concentrations and, after 24 h of incubation, the cells were washed twice with DPBS. Cells were then harvested with trypsin/EDTA and stained with the Annexin V kit following the product instructions. Cells were incubated for 15 min with 5 µL of Annexin V diluted in 200 µL of binding buffer. After 15 min, cells were washed with binding buffer and 5 µL propidium iodide was added prior to flow cytometry analysis. Results were obtained with BD FACSCanto II and analysed by Flow Jo™ v7 software.

Biodistribution analysis. C57BL6 male mice were i.v. with a dose of 0.1 mmol Gd/kg mouse. Biodistribution experiments were performed on a 7 T Bruker Biospec 70/30 USR MRI system (Bruker Biospin GmbH, Ettlingen, Germany), interfaced to an AVANCE III console. A BGA12 imaging gradient (maximum gradient strength 400 mT/m) system with a 40 mm diameter quadrature volume resonator was used for MRI data acquisition. The quantification was performed with T_1-weighted maps. T_1 maps were obtained before and after administration of the nanoparticles by means of a spin echo saturation recovery using a variable repetition time Bruker RAREVTR method. Images were acquired at 8 different TR values 9000, 5000, 3000, 2000, 1500, 1000, 600, 427 ms), effective TE 16 ms, RARE factor 4, 4 averages, 110 x 110 points, a Field of View of 3.2cm x 3.2cm, 10 slices with a slice thickness of 1.0mm and 1.0mm gap between slices. T1 maps were created with "bmg.T1map.SR.v2.py" and reconstructed to a matrix of 128 x 128. The final T_1 maps values were measured by defining different regions of interest (ROIs) for each organ using ITK-SNAP software.

Targeted MRI of atherosclerosis with functionalized CC nanoparticles. NP targeting experiments were performed with four month-old LDLr-/- mice fed a high-fat diet for 4-6 weeks to generate atherosclerosis. For imaging and NP administration, animals were anesthetized first with a mixture of 3-5 % isofluorane and then kept between 1.5-2 % in 50 % O_2. Our nanoprobes were injected into the tail vein at a dose of 0.1 mmol Gd/kg (100 μL) and one hour later 7 T MRI images were acquired in the aortic arch and abdominal regions near the renal bifurcation. To ensure an accurate positioning, pure axial and four-chamber view scout images were used to set up the representative aortic arch view. Images were obtained between the brachiocephalic artery and left common carotid artery, perpendicular to the direction of the flow in the aorta. A single 0.8 mm, 2.8 × 2.8 cm isotropic FOV (obtained and reconstructed with 256 × 256) slice was obtained using a Bruker self-gated cine gradient echo FLASH sequence using the following parameters: minimum TE 4 ms, TR 9 ms, flip angle 10°, 1 average. Additional images in the same position were obtained with a fat suppression module. Aortic renal bifurcation images were acquired with a relaxation enhancement (RARE; fast/turbo spin echo) sequence. 20 slices of 0.8 mm, 32 x 32 mm isotropic FOV (obtained and reconstructed with 256 x 256) were obtained using the following parameters: TE 14 ms, TR 1200 ms, RARE factor= 4, 3 averages. All animal bioimaging experiments were performed in accordance with the Spanish policy for animal protection (RD53/2013), which meets the requirements of the European Union directive 2010/63/ UE, at CIC biomaGUNE animal facility. The procedures were approved by the Ethical Committee of CIC biomaGUNE and authorized by the local authorities (Diputación Foral de Guipúzcoa).

SXRF analysis. Atherosclerotic mice were treated with a single intravenous injection of Gd-doped UCCNPS (0.05 mmol/kg), unlabelled or labelled with different peptides targeting microcalcifications (Alendronate) or inflammation (Trimanose). Saline serum injected mice were used as controls. After 15 or 60 min, the animals were perfused with 4% paraformaldehyde in 0.9% saline solution with heparine (10 U/ml). Their aortas were isolated, cryoprotected using 20% sucrose, embedded in cryo-molds using OCT, and stored at -80º C until sectioned. Then 50 µm thick cross sections were generated and deposited on sapphire discs, and visualized using a brightfield microscope to select areas of the aortas for XRF analysis at the I18 beamline at the Diamond Synchrotron Light Source (Oxford, UK). Both, sections of the arch and renal part of the aortas were obtained.

Irradiation of the samples was carried out using a beam focused at 5x5 μm^2, and energy fixed to 11 keV (flux between 1.6-2.5x10^{11} ph/s). Detection was performed using two 4-element Vortex silicon drift detectors (Hitachi). Scan step size was fixed at 50x50 μm^2 (dwell time 50 ms) for coarse scans to optimize the measurement parameters. Following this, at least 3 high resolution XRF elemental maps were collected for each sample using 5x5 μm^2 scan steps (dwell times 50 ms or 0.5 s). The raw maps were processed using the free PyMCA software.[51] Concentration maps were produced assuming a matrix of 50 µm thick soft tissue, while the quantitative calibration was determined using a thin film x-ray fluorescence 7-element reference sample (AXO Dresden GmbH). The concentration maps were further processed using FIJI ImageJ package.[48]

***In vitro* targeting assays.** The interaction between HAP and our nanoprobes was studied with EDX and ICP-MS. Commercial HAP (200 µL, 1.2 mg/ml) was mixed under stirring with 20 µL of CC-Aln or CC-Trm solutions at [Gd]= 9 mM for 5 and 15 min at 37 ºC. After that, samples were precipitated and washed twice by centrifugation to remove the unattached NPs (10.000 rpm, 10 min). Then, the ratio [Gd]/[Ca] of HAP after incubation and washing steps was measured by EDX and ICP-MS for the two types of NPs. Next, we studied the NP cell uptake with THP-1 derived macrophages. Briefly, human monocytes THP-1 cells were grown in suspension in RPMI with 10% (v/v) fetal bovine serum (FBS), 0.05 mM of β-mercaptoethanol (Sigma Aldrich) and 1% (v:v) antibiotic solution (100 units/mL penicillin, 100 mg/mL streptomycin, P/S) in a humidified 37 °C and 5% CO_2 incubator. THP-1 cells were seeded at 180 000 cells/well in 24 well plates and differentiated to M0 phenotype. They were incubated for 72 h with 150 nM phorbol 12-myristate 13-acetate (PMA)(Sigma-Aldrich), followed by 24 h of incubation with RPMI medium. Then, the macrophages were incubated for 30 min, 2 h and 4 h with CC-Aln and CC-Trm NPs. After the incubation, cells were washed twice with cold DPBS and 150 µL cold RIPA buffer (abcam #ab156034) with protease inhibitor (Fisher scientific # 10320015) was added to each well to lysate the cells. After 30 min incubation on ice 50

μl were collected for protein determination with BCA assay (Thermo Scientific™ 23227) following the product protocol. The rest of the solution (100 μL) was digested with 1 mL of 2% nitric acid for ICP-MS analysis. More details about this section can be found in the SI.

ASSOCIATED CONTENT

AUTHOR INFORMATION

Corresponding authors:

ACKNOWLEDGEMENTS

SCR is supported by the Ministerio de Ciencia e Innovación (PID2019-106139RA-100 and RYC2020-030241-I). CSC acknowledge financial support from the Spanish State Research Agency (grant PID2020-118176RJ-I100), and the Gipuzkoa Foru Aldundia (Gipuzkoa Fellows program; grant number 2019-FELL-000018-01/62/2019). This work was performed under the Severo Ochoa Centers of Excellence Program of the Spanish State Research Agency – Grant No. CEX2018-000867-S (DIPC). XRF analysis was carried out with the support of Diamond Light Source, beamline I18 (proposal SP27720).

REFERENCES

1. Libby, P., The changing landscape of atherosclerosis. *Nature* **2021,** *592* (7855), 524-533.
2. Libby, P.; Buring, J. E.; Badimon, L.; Hansson, G. K.; Deanfield, J.; Bittencourt, M. S.; Tokgözoğlu, L.; Lewis, E. F., Atherosclerosis. *Nature Reviews Disease Primers* **2019,** *5* (1), 56.
3. Lusis, A. J., Atherosclerosis. *Nature* **2000,** *407* (6801), 233-241.
4. Mulder, W. J.; Jaffer, F. A.; Fayad, Z. A.; Nahrendorf, M., Imaging and nanomedicine in inflammatory atherosclerosis. *Sci Transl Med* **2014,** *6* (239), 239sr1.
5. Vigne, J.; Thackeray, J.; Essers, J.; Makowski, M.; Varasteh, Z.; Curaj, A.; Karlas, A.; Canet-Soulas, E.; Mulder, W.; Kiessling, F.; Schäfers, M.; Botnar, R.; Wildgruber, M.; Hyafil, F.; on behalf of the Cardiovascular study group of the European Society of Molecular, I., Current and Emerging Preclinical Approaches for Imaging-Based Characterization of Atherosclerosis. *Molecular Imaging and Biology* **2018,** *20* (6), 869-887.
6. Carregal-Romero, S.; Miguel-Coello, A. B.; Martínez-Parra, L.; Martí-Mateo, Y.; Hernansanz-Agustín, P.; Fernández-Afonso, Y.; Plaza-García, S.; Gutiérrez, L.; Muñoz-Hernández, M. d. M.; Carrillo-Romero, J.; Piñol-Cancer, M.; Lecante, P.; Blasco-Iturri, Z.; Fadón, L.; Almansa-García, A. C.; Möller, M.; Otaegui, D.; Enríquez, J. A.; Groult, H.; Ruíz-Cabello, J., Ultrasmall Manganese Ferrites for In Vivo Catalase Mimicking Activity and Multimodal Bioimaging. *Small* **2022,** *18* (16), 2106570.
7. Ximendes, E.; Benayas, A.; Jaque, D.; Marin, R., Quo Vadis, Nanoparticle-Enabled In Vivo Fluorescence Imaging? *ACS Nano* **2021,** *15* (2), 1917-1941.
8. Pellico, J.; Lechuga-Vieco, A. V.; Almarza, E.; Hidalgo, A.; Mesa-Nuñez, C.; Fernández-Barahona, I.; Quintana, J. A.; Bueren, J.; Enríquez, J. A.; Ruiz-Cabello, J.; Herranz, F., In vivo imaging of lung inflammation with neutrophil-specific 68Ga nano-radiotracer. *Scientific Reports* **2017,** *7* (1), 13242.
9. Dong, Y. C.; Hajfathalian, M.; Maidment, P. S. N.; Hsu, J. C.; Naha, P. C.; Si-Mohamed, S.; Breuilly, M.; Kim, J.; Chhour, P.; Douek, P.; Litt, H. I.; Cormode, D. P., Effect of Gold Nanoparticle Size on Their Properties as Contrast Agents for Computed Tomography. *Scientific Reports* **2019,** *9* (1), 14912.

10. Zhang, M.; Xie, Z.; Long, H.; Ren, K.; Hou, L.; Wang, Y.; Xu, X.; Lei, W.; Yang, Z.; Ahmed, S.; Zhang, H.; Zhao, G., Current advances in the imaging of atherosclerotic vulnerable plaque using nanoparticles. *Materials Today Bio* **2022,** *14*, 100236.
11. Lobatto, M. E.; Calcagno, C.; Millon, A.; Senders, M. L.; Fay, F.; Robson, P. M.; Ramachandran, S.; Binderup, T.; Paridaans, M. P.; Sensarn, S.; Rogalla, S.; Gordon, R. E.; Cardoso, L.; Storm, G.; Metselaar, J. M.; Contag, C. H.; Stroes, E. S.; Fayad, Z. A.; Mulder, W. J., Atherosclerotic plaque targeting mechanism of long-circulating nanoparticles established by multimodal imaging. *ACS Nano* **2015,** *9* (2), 1837-47.
12. Sanchez-Gaytan, B. L.; Fay, F.; Lobatto, M. E.; Tang, J.; Ouimet, M.; Kim, Y.; van der Staay, S. E. M.; van Rijs, S. M.; Priem, B.; Zhang, L.; Fisher, E. A.; Moore, K. J.; Langer, R.; Fayad, Z. A.; Mulder, W. J. M., HDL-Mimetic PLGA Nanoparticle To Target Atherosclerosis Plaque Macrophages. *Bioconjugate Chem.* **2015,** *26* (3), 443-451.
13. Yin, T.; Li, Y.; Ren, Y.; Fuad, A. R. M.; Hu, F.; Du, R.; Wang, Y.; Wang, G.; Wang, Y., Phagocytosis of polymeric nanoparticles aided activation of macrophages to increase atherosclerotic plaques in ApoE−/− mice. *Journal of Nanobiotechnology* **2021,** *19* (1), 121.
14. Kim, M.; Sahu, A.; Kim, G. B.; Nam, G. H.; Um, W.; Shin, S. J.; Jeong, Y. Y.; Kim, I. S.; Kim, K.; Kwon, I. C.; Tae, G., Comparison of in vivo targeting ability between cRGD and collagen-targeting peptide conjugated nano-carriers for atherosclerosis. *J Control Release* **2018,** *269*, 337-346.
15. Pellico, J.; Fernández-Barahona, I.; Ruiz-Cabello, J.; Gutiérrez, L.; Muñoz-Hernando, M.; Sánchez-Guisado, M. J.; Aiestaran-Zelaia, I.; Martínez-Parra, L.; Rodríguez, I.; Bentzon, J.; Herranz, F., HAP-Multitag, a PET and Positive MRI Contrast Nanotracer for the Longitudinal Characterization of Vascular Calcifications in Atherosclerosis. *ACS Applied Materials & Interfaces* **2021,** *13* (38), 45279-45290.
16. Metselaar, J. M.; Lammers, T., Challenges in nanomedicine clinical translation. *Drug delivery and translational research* **2020,** *10* (3), 721-725.
17. Niu, Y.-Q.; Liu, J.-H.; Aymonier, C.; Fermani, S.; Kralj, D.; Falini, G.; Zhou, C.-H., Calcium carbonate: controlled synthesis, surface functionalization, and nanostructured materials. *Chemical Society Reviews* **2022,** *51* (18), 7883-7943.
18. Rodriguez-Blanco, J. D.; Shaw, S.; Benning, L. G., The kinetics and mechanisms of amorphous calcium carbonate (ACC) crystallization to calcite, viavaterite. *Nanoscale* **2011,** *3* (1), 265-271.
19. Huang, S.-C.; Naka, K.; Chujo, Y., A Carbonate Controlled-Addition Method for Amorphous Calcium Carbonate Spheres Stabilized by Poly(acrylic acid)s. *Langmuir* **2007,** *23* (24), 12086-12095.
20. Jia, X.; Kayitmazer, A. B.; Ahmad, A.; Ramzan, N.; Li, Y.; Xu, Y.; Sun, S., Polyacids for producing colloidally stable amorphous calcium carbonate clusters in water. *Journal of Applied Polymer Science* **2022,** *139* (14), 51899.
21. Liang, G.; Cao, L.; Chen, H.; Zhang, Z.; Zhang, S.; Yu, S.; Shen, X.; Kong, J., Ultrasmall gadolinium hydrated carbonate nanoparticle: an advanced T1 MRI contrast agent with large longitudinal relaxivity. *Journal of Materials Chemistry B* **2013,** *1* (5), 629-638.
22. Dong, L.; Xu, Y. J.; Sui, C.; Zhao, Y.; Mao, L. B.; Gebauer, D.; Rosenberg, R.; Avaro, J.; Wu, Y.-D.; Gao, H.-L.; Pan, Z.; Wen, H. Q.; Yan, X.; Li, F.; Lu, Y.; Cölfen, H.; Yu, S.-H., Highly hydrated paramagnetic amorphous calcium carbonate nanoclusters as an MRI contrast agent. *Nature Communications* **2022,** *13* (1), 5088.
23. VanderSchee, C. R.; Kuter, D.; Chou, H.; Jackson, B. P.; Mann, K. K.; Bohle, D. S., Addressing K/L-edge overlap in elemental analysis from micro-X-ray fluorescence: bioimaging of tungsten and zinc in bone tissue using synchrotron radiation and laser ablation inductively coupled plasma mass spectrometry. *Analytical and Bioanalytical Chemistry* **2020,** *412* (2), 259-265.
24. Moore, K. J.; Tabas, I., Macrophages in the pathogenesis of atherosclerosis. *Cell* **2011,** *145* (3), 341-55.

25. Chen, P. S.; Toribara, T. Y.; Warner, H., Microdetermination of Phosphorus. *Analytical Chemistry* **1956,** *28* (11), 1756-1758.
26. Donnelly, F. C.; Purcell-Milton, F.; Framont, V.; Cleary, O.; Dunne, P. W.; Gun'ko, Y. K., Synthesis of CaCO3 nano- and micro-particles by dry ice carbonation. *Chem. Commun.* **2017,** *53* (49), 6657-6660.
27. Gunasekaran, S.; Anbalagan, G.; Pandi, S., Raman and infrared spectra of carbonates of calcite structure. *Journal of Raman Spectroscopy* **2006,** *37* (9), 892-899.
28. Young, A. M.; Sherpa, A.; Pearson, G.; Schottlander, B.; Waters, D. N., Use of Raman spectroscopy in the characterisation of the acid-base reaction in glass-ionomer cements. *Biomaterials* **2000,** *21* (19), 1971-9.
29. Liu, X.; Qu, S.; Lu, X.; Ge, X.; Leng, Y., Time-of-flight secondary ion mass spectrometry study on the distribution of alendronate sodium in drug-loaded ultra-high molecular weight polyethylene. *Biomedical materials (Bristol, England)* **2009,** *4* (6), 065008.
30. Aime, S.; Caravan, P., Biodistribution of gadolinium-based contrast agents, including gadolinium deposition. *Journal of magnetic resonance imaging : JMRI* **2009,** *30* (6), 1259-67.
31. Wei, H.; Bruns, O. T.; Kaul, M. G.; Hansen, E. C.; Barch, M.; Wiśniowska, A.; Chen, O.; Chen, Y.; Li, N.; Okada, S.; Cordero, J. M.; Heine, M.; Farrar, C. T.; Montana, D. M.; Adam, G.; Ittrich, H.; Jasanoff, A.; Nielsen, P.; Bawendi, M. G., Exceedingly small iron oxide nanoparticles as positive MRI contrast agents. *Proceedings of the National Academy of Sciences* **2017,** *114* (9), 2325-2330.
32. García-Soriano, D.; Amaro, R.; Lafuente-Gómez, N.; Milán-Rois, P.; Somoza, Á.; Navío, C.; Herranz, F.; Gutiérrez, L.; Salas, G., The influence of cation incorporation and leaching in the properties of Mn-doped nanoparticles for biomedical applications. *Journal of Colloid and Interface Science* **2020**.
33. Amiri, H.; Bordonali, L.; Lascialfari, A.; Wan, S.; Monopoli, M. P.; Lynch, I.; Laurent, S.; Mahmoudi, M., Protein corona affects the relaxivity and MRI contrast efficiency of magnetic nanoparticles. *Nanoscale* **2013,** *5* (18), 8656-8665.
34. Ta, H. T.; Li, Z.; Wu, Y.; Cowin, G.; Zhang, S.; Yago, A.; Whittaker, A. K.; Xu, Z. P., Effects of magnetic field strength and particle aggregation on relaxivity of ultra-small dual contrast iron oxide nanoparticles. *Materials Research Express* **2017,** *4* (11), 116105.
35. Li, H.; Meade, T. J., Molecular Magnetic Resonance Imaging with Gd(III)-Based Contrast Agents: Challenges and Key Advances. *Journal of the American Chemical Society* **2019,** *141* (43), 17025-17041.
36. Liang, X.; Dempski, R. E.; Burdette, S. C., Zn(2+) at a cellular crossroads. *Current opinion in chemical biology* **2016,** *31*, 120-5.
37. Sanford, L.; Carpenter, M. C.; Palmer, A. E., Intracellular Zn2+ transients modulate global gene expression in dissociated rat hippocampal neurons. *Scientific Reports* **2019,** *9* (1), 9411.
38. Maret, W., Molecular aspects of human cellular zinc homeostasis: redox control of zinc potentials and zinc signals. *Biometals* **2009,** *22* (1), 149-57.
39. Liu, C. L.; Zhang, X.; Liu, J.; Wang, Y.; Sukhova, G. K.; Wojtkiewicz, G. R.; Liu, T.; Tang, R.; Achilefu, S., Na(+)-H(+) exchanger 1 determines atherosclerotic lesion acidification and promotes atherogenesis. **2019,** *10* (1), 3978.
40. Chin, D. D.; Chowdhuri, S.; Chung, E. J., Calcium-Binding Nanoparticles for Vascular Disease. *Regenerative Engineering and Translational Medicine* **2019,** *5* (1), 74-85.
41. He, H.; Wang, J.; Yannie, P. J.; Korzun, W. J.; Yang, H.; Ghosh, S., Nanoparticle-based "Two-pronged" approach to regress atherosclerosis by simultaneous modulation of cholesterol influx and efflux. *Biomaterials* **2020,** *260*, 120333.
42. Getz, G. S.; Reardon, C. A., Do the Apoe-/- and Ldlr-/- Mice Yield the Same Insight on Atherogenesis? *Arteriosclerosis, thrombosis, and vascular biology* **2016,** *36* (9), 1734-41.

43. Sijbers, J.; Scheunders, P.; Bonnet, N.; Van Dyck, D.; Raman, E., Quantification and improvement of the signal-to-noise ratio in a magnetic resonance image acquisition procedure. *Magnetic resonance imaging* **1996,** *14* (10), 1157-1163.
44. Sanchez-Cano, C.; Alvarez-Puebla, R. A.; Abendroth, J. M.; Beck, T.; Blick, R.; Cao, Y.; Caruso, F.; Chakraborty, I.; Chapman, H. N.; Chen, C.; Cohen, B. E.; Conceição, A. L. C.; Cormode, D. P.; Cui, D.; Dawson, K. A.; Falkenberg, G.; Fan, C.; Feliu, N.; Gao, M.; Gargioni, E.; Glüer, C.-C.; Grüner, F.; Hassan, M.; Hu, Y.; Huang, Y.; Huber, S.; Huse, N.; Kang, Y.; Khademhosseini, A.; Keller, T. F.; Körnig, C.; Kotov, N. A.; Koziej, D.; Liang, X.-J.; Liu, B.; Liu, S.; Liu, Y.; Liu, Z.; Liz-Marzán, L. M.; Ma, X.; Machicote, A.; Maison, W.; Mancuso, A. P.; Megahed, S.; Nickel, B.; Otto, F.; Palencia, C.; Pascarelli, S.; Pearson, A.; Peñate-Medina, O.; Qi, B.; Rädler, J.; Richardson, J. J.; Rosenhahn, A.; Rothkamm, K.; Rübhausen, M.; Sanyal, M. K.; Schaak, R. E.; Schlemmer, H.-P.; Schmidt, M.; Schmutzler, O.; Schotten, T.; Schulz, F.; Sood, A. K.; Spiers, K. M.; Staufer, T.; Stemer, D. M.; Stierle, A.; Sun, X.; Tsakanova, G.; Weiss, P. S.; Weller, H.; Westermeier, F.; Xu, M.; Yan, H.; Zeng, Y.; Zhao, Y.; Zhao, Y.; Zhu, D.; Zhu, Y.; Parak, W. J., X-ray-Based Techniques to Study the Nano–Bio Interface. *ACS Nano* **2021,** *15* (3), 3754-3807.
45. Aires, A.; Maestro, D.; Ruiz del Rio, J.; Palanca, A. R.; Lopez-Martinez, E.; Llarena, I.; Geraki, K.; Sanchez-Cano, C.; Villar, A. V.; Cortajarena, A. L., Engineering multifunctional metal/protein hybrid nanomaterials as tools for therapeutic intervention and high-sensitivity detection. *Chemical Science* **2021,** *12* (7), 2480-2487.
46. Sanchez-Cano, C.; Romero-Canelón, I.; Yang, Y.; Hands-Portman, I. J.; Bohic, S.; Cloetens, P.; Sadler, P. J., Synchrotron X-Ray Fluorescence Nanoprobe Reveals Target Sites for Organo-Osmium Complex in Human Ovarian Cancer Cells. *Chemistry – A European Journal* **2017,** *23* (11), 2512-2516.
47. Lo, M. N.; Damon, L. J.; Wei Tay, J.; Jia, S.; Palmer, A. E., Single cell analysis reveals multiple requirements for zinc in the mammalian cell cycle. *eLife* **2020,** *9*, e51107.
48. Schindelin, J.; Arganda-Carreras, I.; Frise, E.; Kaynig, V.; Longair, M.; Pietzsch, T.; Preibisch, S.; Rueden, C.; Saalfeld, S.; Schmid, B.; Tinevez, J.-Y.; White, D. J.; Hartenstein, V.; Eliceiri, K.; Tomancak, P.; Cardona, A., Fiji: an open-source platform for biological-image analysis. *Nature Methods* **2012,** *9* (7), 676-682.
49. Coffman, A. A.; Basta-Pljakic, J.; Guerra, R. M.; Ebetino, F. H.; Lundy, M. W.; Majeska, R. J.; Schaffler, M. B., A Bisphosphonate With a Low Hydroxyapatite Binding Affinity Prevents Bone Loss in Mice After Ovariectomy and Reverses Rapidly With Treatment Cessation. *JBMR Plus* **2021,** *5* (4), e10476.
50. Lin, T.-J., Predicting binding affinities of nitrogen-containing bisphosphonates on hydroxyapatite surface by molecular dynamics. *Chemical Physics Letters* **2019,** *716*, 83-92.
51. Solé, V. A.; Papillon, E.; Cotte, M.; Walter, P.; Susini, J., A multiplatform code for the analysis of energy-dispersive X-ray fluorescence spectra. *Spectrochimica Acta Part B: Atomic Spectroscopy* **2007,** *62* (1), 63-68.